

Geophysical Research Letters



RESEARCH LETTER

10.1029/2020GL092261

Key Points:

- In late 2018, the Visible Infrared Imaging Radiometer Suite sensor recorded a temperature of 161.96K associated with a convective storm in the tropical West Pacific
- An extremely cold tropopause coupled to an energetic overshooting top produced this cloud top temperature
- An 18-year data set of satellite observations suggest that such cold cloud top temperatures may be becoming more common

Supporting Information:

- Supporting Information S1
- Figure S1
- Figure S2
- Movie S1
- Movie S2

Correspondence to:

S. R. Proud,
simon.proud@physics.ox.ac.uk

Citation:

Proud, S. R., & Bachmeier, S. (2021). Record-low cloud temperatures associated with a tropical deep convective event. *Geophysical Research Letters*, 48, e2020GL092261. <https://doi.org/10.1029/2020GL092261>

Received 22 DEC 2020

Accepted 18 FEB 2021

© 2021. The Authors.

This is an open access article under the terms of the [Creative Commons Attribution](#) License, which permits use, distribution and reproduction in any medium, provided the original work is properly cited.

Record-Low Cloud Temperatures Associated With a Tropical Deep Convective Event

Simon Richard Proud^{1,2}  and Scott Bachmeier³

¹National Centre for Earth Observation, Oxford, UK, ²Sub-Department of Atmospheric, Oceanic and Planetary Physics, University of Oxford, Oxford, UK, ³Cooperative Institute for Meteorological Satellite Studies, University of Wisconsin—Madison, Madison, WI, USA

Abstract Earth-orbiting satellites have long been used to examine meteorological processes. In the context of severe weather, brightness temperatures (BTs) at infrared wavelengths allow the determination of convective cloud properties. The anvils of cumulonimbus clouds, for example, typically produce BTs close to the tropopause temperature. Particularly severe storms generate overshoots that penetrate the stratosphere and are cooler than the anvil. In this study, we describe clustered storm overshoots in the tropical West Pacific on December 29, 2018 that resulted in the Visible Infrared Imaging Radiometer Suite (VIIRS) aboard NOAA-20 measuring a temperature of 161.96K (−111.2°C), which is, to our knowledge, the coldest on record. We describe the local meteorological conditions, examine the VIIRS overpass that produced the cold temperature, compare VIIRS with other sensors that observed the region and, finally, analyze the historical context provided by two other satellite instruments to show that such cold temperatures may be becoming more common.

Plain Language Summary Satellites orbiting the Earth often carry infrared sensors that measure the temperature of the Earth and its atmosphere. When viewing a thunderstorm, tropical cyclone, or other form of severe convective weather these sensors will record a very cold temperature, as the clouds that form these storms are typically at high altitude and are hence well below freezing. In this study, we examine a case in which one sensor, the Visible Infrared Imaging Radiometer Suite, measured an extremely cold temperature that is, to our knowledge, the coldest recorded by satellite. We discuss this measurement, placing it in the historical context, analyzing the storm that produced the temperature and discussing how noise and sensor calibration may affect the measurement.

1. Introduction

Convection, the lifting of warm air from low altitude to higher altitudes, is a key meteorological process and is responsible for much of our hazardous weather, such as lightning, hail, and extreme rainfall (Doswell, 2001). Isolated convective cells are common around the globe, often taking on a characteristic “anvil” shape whereby the air in the storm updraft meets the natural temperature inversion at the tropopause and spreads horizontally to form a large cloud with a relatively flat top. If the updraft is strong enough, it can push through the tropopause into the lower stratosphere in the form of an overshooting top (OT) that can protrude several kilometers above the anvil, depending on updraft strength. While overshoots are usually only a few km in width, they indicate a particularly severe storm and have thus been used as a predictor of hazardous weather. An OT will continue cooling as it rises, and in satellite images will therefore appear cooler than the surrounding anvil, as well as cooler than the stratospheric air in which it now resides (Sun et al., 2018). But in some cases an overshoot can produce a cirrus plume: A thin layer of ice cloud in the stratosphere that is blown downwind of the OT and warms to stratospheric temperature. In satellite images, these plumes present as a region warmer than the anvil that extends from an OT (Bedka et al., 2018).

On a regional scale, multiple convective cells may begin to organize to produce a mesoscale convective system, and if the location and conditions are suitable (such as over warm open water), then the organized cluster of convection will begin to rotate, forming a tropical cyclone. The Western Pacific is a key location for both convective organization and the development of powerful cyclones due to warm sea surface temperatures and atmospheric temperature and humidity profiles that favor convection. The tropopause in this region is also particularly high, and hence cold, and therefore allows significant vertical development

of storms. During December and January, the intertropical convergence zone reaches its most Southerly extent, which further encourages convective development in the South Pacific (Basher & Zheng, 1995).

Weather satellites in GEostationary Orbit (GEO) are a key tool in monitoring the tropical Pacific region, especially as ground-based radar coverage is not available for the majority of the area. Geostationary satellite provides full coverage of the tropics, with each satellite observing up to 30% of the Earth's surface at a given time. These satellites carry imaging sensors that passively observe the Earth, measuring reflected sunlight in the visible spectrum and emitted radiance in the infrared spectrum. Various meteorological agencies operate these satellites, with each having different characteristics and performance. In general, geostationary sensors produce new images of their coverage area every 10–15 min (100–150 images per day) in 3–5 visible and 5–10 infrared “channels” that cover specific spectral regions. Spatial resolution varies but can be as high as 0.5 km per pixel in the visible and is typically 2–4 km in the infrared (Aminou, 2002; Bessho et al., 2016; Hong et al., 2016). Convective clouds will appear bright in visible channels, due to the highly reflective cloud tops, and very cold in the infrared as these clouds are at (or in the case of OTs, below) the tropopause temperature, which is usually 180–220K depending on location.

Complementary to the geostationary sensors that provide high temporal resolution at relatively low spatial resolution, Low Earth Orbit (LEO) satellites typically have a much higher spatial resolution (better than 1 km in both visible and infrared wavelengths) but with a lower temporal resolution, typically providing only one or two views of a location per day (Schueler et al., 2002). These LEO data allow better examination of small-scale features within a storm, such as OTs and is often also better calibrated than GEO data, allowing more accurate cloud temperatures to be retrieved. In this study, we combine LEO data from the VIIRS, Moderate Resolution Imaging Spectroradiometer (MODIS; Barnes et al., 2003), Advanced Very-High-Resolution Radiometer (AVHRR; Teillet et al., 1990), and Sea and Land Surface Temperature Radiometer (SLSTR; Coppo et al., 2010) sensors with GEO data from the Advanced Himawari Imager (AHI), Advanced Baseline Imager (ABI; Schmit et al., 2017), and Advanced Geosynchronous Radiation Imager (AGRI; Zhu et al., 2020) sensors (Table ST1) to examine the particularly cold temperatures recorded in late 2018, as shown in Figure 1.

2. Meteorological Overview

The area of the South Western Pacific in which VIIRS measured the cold cloud top temperature is associated with a very cold tropopause, averaging 189K in the ERA5 climatology between 2002 and 2020 (Hersbach et al., 2020), and hence allows deep convective storms to reach particularly cold temperatures. As shown in Figure 2, on the day of this event the tropopause was substantially colder than average: Approximately 176K according to analysis of the ERA5 profile. In addition, low wind shear (see supplementary Figure S1) and warm sea surface temperatures of 302K–304K encourage convective development. However, the lower troposphere was only modestly conducive to convection with convective available potential energy (CAPE) values of between 300 and 1,100 J/Kg in the hours preceding the VIIRS overpass.

As shown in Figure S2, beginning at 07:00 UTC (~18:00 local solar time) a significant number of convective cells developed in the region between 163° and 165°E along the 4°S line of latitude. These cells were short-lived but produced multiple OTs, corresponding to a general reduction in the minimum observed BT shown in Figure 3. At 10:00 UTC, a cluster of deep convective storms developed in the East of the area, triggering further development spreading Westwards and, by 12:30, energetic OTs that cooled significantly below the tropopause temperature. Based on the data from the AHI sensor, had VIIRS flown over the area at this time there is a strong possibility that it would have recorded even lower BTs than during its actual overpass one hour later.

Over the next 4 h, continued deep overshoots occurred in the storm cluster while a growing cirrus cloud shield extended to cover a 2° latitude by 4° longitude through which OTs, including those observed by VIIRS, protruded. By 16:30 a large region of cloud tops below the estimated tropopause temperature had formed, possibly indicating the presence of a double tropopause due to cooling caused by the interaction of material in the OTs with the initially warm stratosphere. By 19:00 UTC, convection began to die down, although much of the area remained covered by cirrus remnants from the convective anvils.

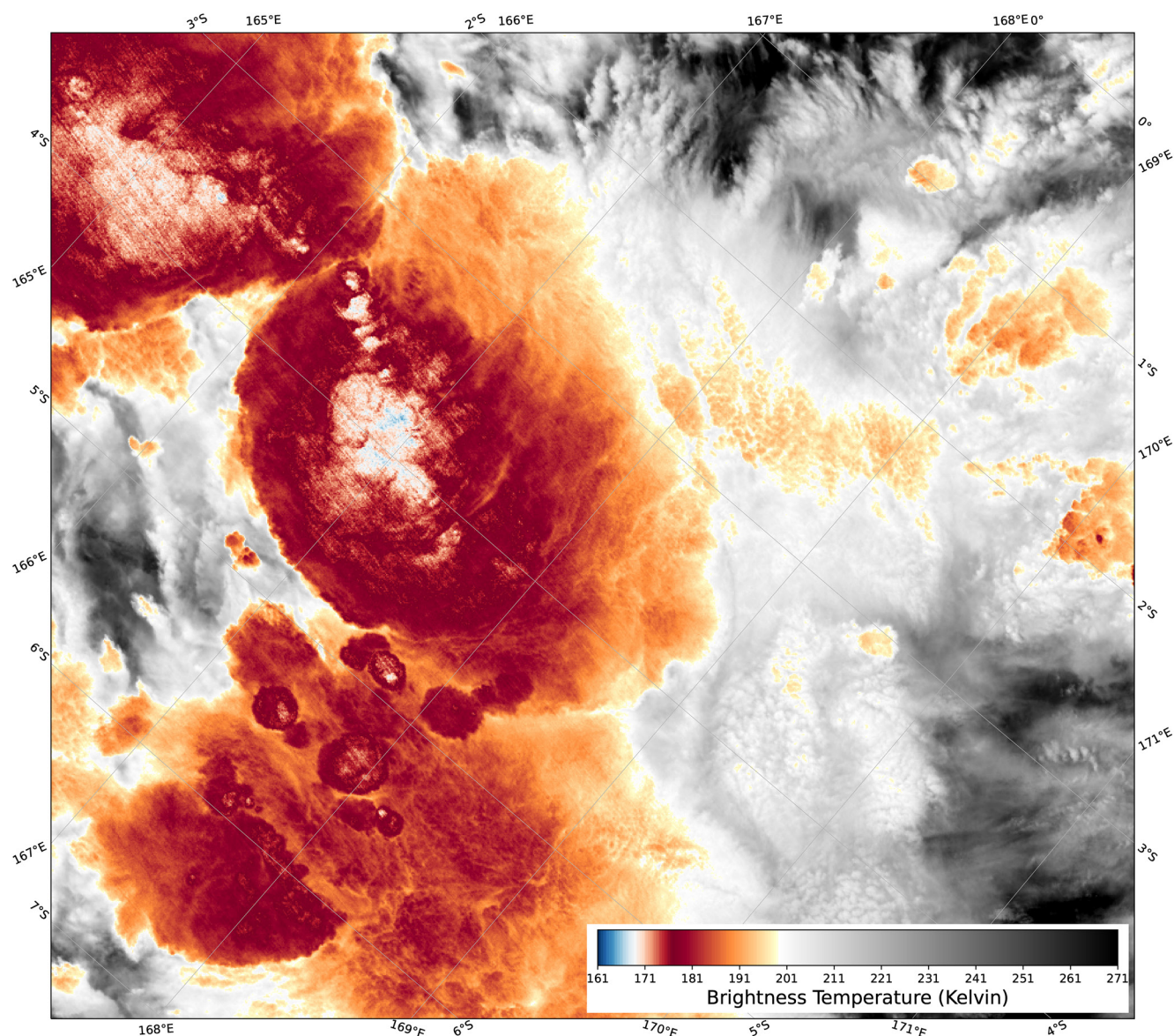


Figure 1. VIIRS I5 brightness temperatures (BTs) for 13:38 UTC on December 29, 2018. The cluster of particularly cold BTs is slightly to the left of the image center. VIIRS, Visible Infrared Imaging Radiometer Suite.

Based on 4 years of AHI data, storm activity on this day was typical for the time of year, implying that the cold cloud top temperatures were primarily driven by the exceptionally cold tropopause rather than the unique properties of a given convective storm. This contrasts with other reported cold temperatures such as in Typhoon Kammuri, where a temperature of 163.75K was recorded, 2K warmer than this case, but with a much warmer tropopause temperature of 185K (Bachmeier, 2019).

3. VIIRS Satellite Measurements

Throughout its lifetime, the region of convection that generated the extremely cold BT shown in 1 was within the field-of-view of three geostationary sensors: AHI on Himawari-8, ABI on GOES-17, and AGRI on Fengyun-4A. For all three sensors the region was seen in “full disk” imagery at the nominal temporal resolution of one image every 10 min. AHI and GOES also have a “mesoscale” sector that produces rapid-update images for a small region, typically impactful severe weather, but neither satellite’s mesoscale sectors observed the region of interest here. In this study, we focus on the infrared channel for each sensor that

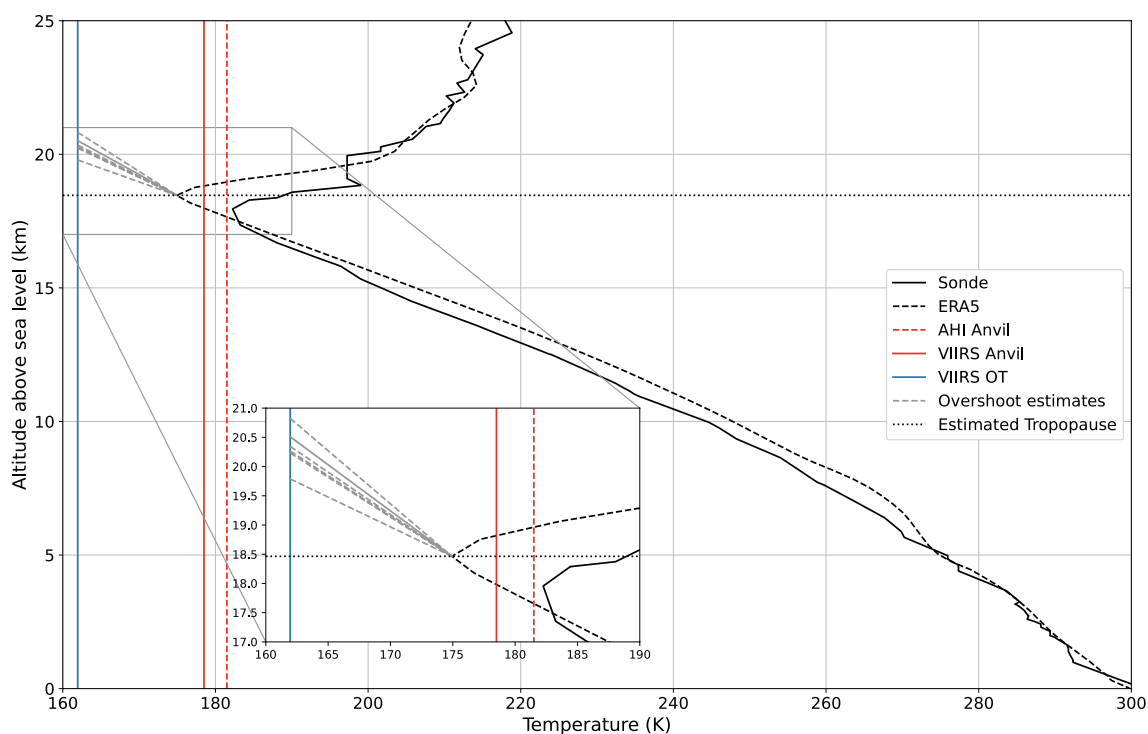


Figure 2. Atmospheric temperature sounding in the region of the convective overshoot. The nearest radiosonde measurement (Koror, Palau, 6.99°N, 158.21°E, ~1.200 km away) is shown as the black solid line. The ECMWF ERA5 profile is shown as the black dashed line. The two vertical red lines indicate cloud anvil temperatures from co-temporal VIIRS and AHI data, and the blue line denotes the measured VIIRS BT. The horizontal dotted line indicates tropopause altitude derived from the ERA5 profile while the five gray dashed lines represent OT altitude estimates based on various above-tropopause lapse rates, as defined in the supplementary material. AHI, Advanced Himawari Imager; BT, brightness temperature; VIIRS, Visible Infrared Imaging Radiometer Suite.

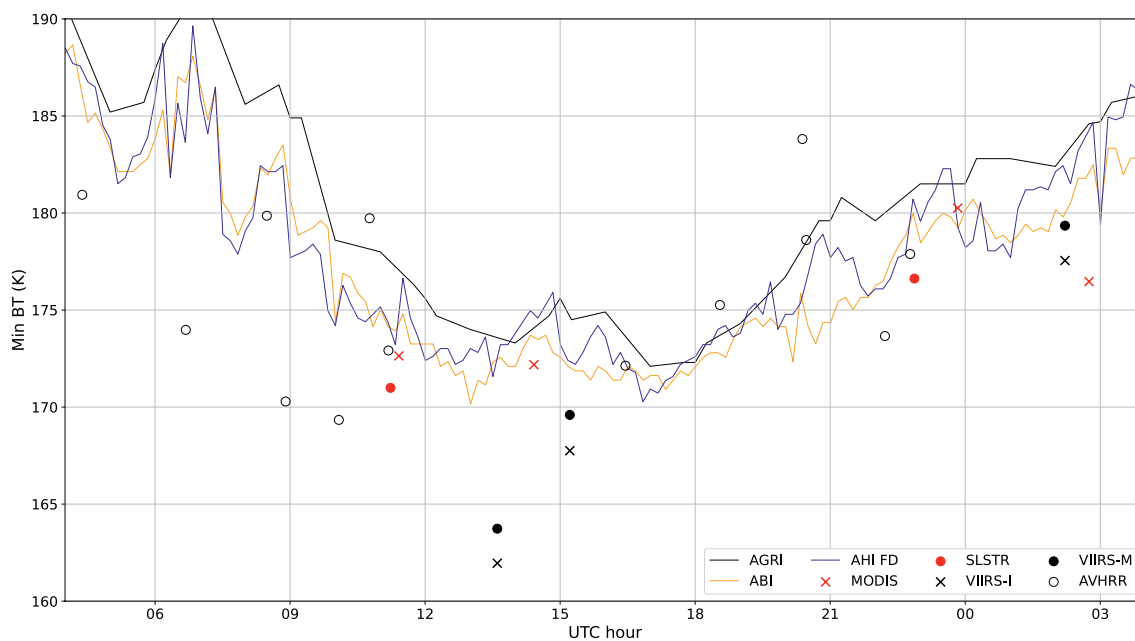


Figure 3. A time series of minimum brightness temperatures (BTs) measured by various sensors in a $4 \times 4^\circ$ box centered on the cold BT between 04:00 UTC on December 29, and 04:00 UTC on December 30, 2018. The AGRI data contains many missing timesteps, and hence looks smoother than the more rapidly updating AHI and ABI temperature traces. ABI, Advanced Baseline Imager; AGRI, Advanced Geosynchronous Radiation Imager; AHI, Advanced Himawari Imager; BT, brightness temperature.

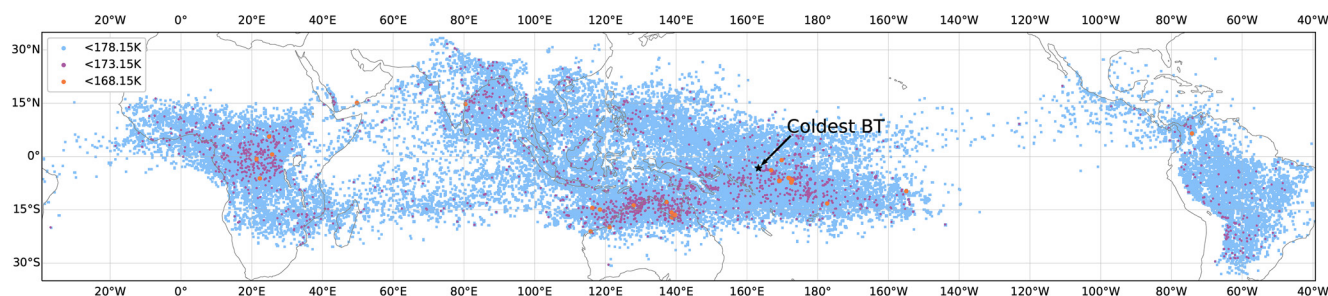


Figure 4. A map of all particularly cold brightness temperatures (BTs) recorded by the MODIS instrument aboard NASA's Aqua satellite between August 2004 and August 2020. The location of the cold BT discussed in this study is shown by the red star. Areas outside 30° North/South latitude are excluded, as no extreme cold BTs were recorded there. Similar, regional, data for AHI is shown in Figure S4. AHI, Advanced Himawari Imager; BT, brightness temperature.

has a central wavelength closest to 11 μm , an atmospheric window channel in which gaseous absorption is minimal (Zhou & Cheng, 2020). Various LEO sensors also observed this region on a semi-regular basis, and we begin by focusing on the VIIRS instrument's high spatial resolution I5 channel. The Satpy tool (Raspaud et al., 2018) was used for loading, calibrating and processing all satellite data used in this manuscript, further details are given in the supporting information S2.

At $\sim 13:38$ UTC on December 29, 2018, the VIIRS aboard the NOAA-20 spacecraft imaged the region of significant convective activity shown in Figure 1. Anvil clouds are the orange/red regions, with temperatures between 175 and 185K, and sensor noise is visible on the top left anvil as faint diagonal banding, which shows a variation in temperature of $\pm 2\text{K}$. Slightly to the left of center, at 3.26°S and 163.25°E , is a blue cluster denoting BTs below 168K. In this cluster are multiple pixels below 164K, including one pixel at 161.96K.

Atmospheric temperature profiles from a radiosonde and the ERA5 reanalysis are shown in 2. Estimates of the tropopause derived from the mean anvil cloud temperature in the VIIRS I5 and AHI B14 channels are shown as red lines and are relatively similar: AHI is $\sim 3\text{K}$ warmer than VIIRS, which is primarily due to the VIIRS data reporting both more numerous and colder OTs thanks to its improved spatial resolution. The dashed lines denote estimates of overshooting from a range of lapse rates, see Table S2. All lapse rates indicate an overshoot that protruded at least 1.3 km above the underlying anvil cloud.

The 161.96K overshoot is, to our knowledge, the coldest recorded satellite BT. In the literature, a BT of 170.9K was detected in Tropical Cyclone Hilda in 1992 (Ebert & Holland, 1992). The VIIRS sensor was also reported to have measured a temperature of 163.75K while overflying Typhoon Kammuri in 2019 (Bachmeier, 2019). Our own (incomplete) record of satellite data shows that BTs between 165K and 168K have been sporadically recorded by the MODIS (as shown in Figure 4 and VIIRS [not shown]) instruments during their lifetimes. All of these are, however, warmer than the temperature reported here.

This temperature has a significant uncertainty associated with it, though, as VIIRS is not well calibrated for such low temperatures. Because of the uniqueness of these temperatures, there is little information available in order to make an accurate estimate of the uncertainty, but we can generally split the uncertainty into three components:

3.1. Instrument Noise (Smith et al., 2020)

VIIRS does not directly measure temperature, but rather the outgoing radiance in a pixel, which is very low at cold temperatures. Typically, an instrument will have a radiance noise that is relatively independent of scene temperature, meaning that at low radiances the noise is proportionately larger relative to the observation. At 210K, the noise equivalent delta temperature (NEDT) for the VIIRS I5 band is 0.32K. Assuming the noise is independent of temperature, at 162K the NEDT will be $\sim 1.8\text{K}$ (Li, Xiong, McIntire, Angal, et al., 2018).

3.2. Data Representation (Angal et al., 2018)

The radiance measured by the sensor is converted into a 12-bit digital representation for transmission to the ground. This conversion results in a loss of precision that is dependent upon temperature: a change of ± 1 in the digital number results in a larger change in BT for cold pixels than for warmer pixels due to the relative importance of a small change in the radiance. At 162K, the analog-to-digital conversion process results in a delta-BT of ~ 0.75 K.

3.3. Calibration Uncertainty

A set of calibration coefficients are used to transform the measured signal into a radiance value. These coefficients are based on pre-launch tests against a calibration target. On orbit, they are adjusted through measurements of an onboard black body, which is around 267K for VIIRS (Li, Xiong, McIntire, & Wu, 2018), and deep space that presents a radiance of near-zero. As no specific calibration has been performed for the temperatures discussed in this study, it is hard to estimate the uncertainty in the calibration, but due to the use of a deep space target we expect it to be small. Overall, an uncertainty of ± 2.7 K is a reasonable assumption (private communication with VIIRS calibration team). Therefore, even at the warm end of this range, the cold OT we discuss here is most likely still cooler than non-VIIRS previous low BT measurements discussed in the literature and is also cooler than the VIIRS measurement of 163.8K in Typhoon Kammuri.

4. Intra-satellite Comparison

To gain a broader perspective, 3 shows satellite-measured BTs over an 18 h period centered on the extreme BT measured by VIIRS. The figure shows that the VIIRS-I band temperatures are significantly colder (>10 K) than those measured by other sensors and somewhat colder (~ 1.7 K) than the corresponding VIIRS-M band temperature. Figure S3 provides additional information, showing the temperatures measured by various sensors overlaid on a simulated infrared spectra, emphasizing the need for considering the spectral response of bands near absorption features. The I-band is almost clear of absorption features and has twice the spatial resolution of the M-band (375 vs. 750 m) plus significantly higher resolution than the three geostationary sensors (2 km+). Resampling the I-band data onto the spatial grids of the lower resolution sensors produces temperatures that match more closely, with differences of 0.2K for M-band, ~ 1.5 K for AHI and ABI, and 2.1K for AGRI. The three other LEO sensors, MODIS, AVHRR, and SLSTR, have a 1 km spatial resolution and typically report BTs somewhat lower than those from the GEO sensors. This highlights the importance of high spatial resolution measurements for examining cloud top structure and OTs in particular: Analysis of the 350 m resolution VIIRS data shows that the OT itself is ~ 9 VIIRS pixels or 1.27 km² with an average temperature of 163.9K. The residual intra-sensor differences are primarily due to the time of measurement: As shown by AHI and ABI, the minimum BT varies rapidly, and hence a difference in measurement time of only a few minutes can result in a change in temperature of several Kelvin. The nearest AHI and ABI measurements were ~ 3 min earlier than VIIRS, and hence it is likely that the VIIRS overpass was fortuitously timed to capture the peak of the cold OT that was not captured by the GEO sensors.

The three geostationary instruments show a good correlation over time, and highlight the importance of rapidly updating data for monitoring convective development that adds considerable value to the high spatial resolution LEO data. In this case, the coldest measurements made by ABI and AHI were, respectively, 30 min earlier and 4 h later than the VIIRS overpass.

5. Historical Perspective

The MODIS sensor aboard NASA's Aqua and Terra spacecraft provides an excellent long-term record of BTs. To examine the historical frequency of extremely low BTs, we analyzed the MODIS/Aqua data between 2004 and 2020, as shown in Figure 4. This shows that the Eastern Pacific and the Atlantic see very few cold (<178 K) BTs, whilst such temperatures are relatively common in the cloud tops over Central Africa, the Western Pacific, Bay of Bengal, and Northern coast of Australia. Overall, 95.6% of extremely cold BTs (<168 K) recorded by MODIS occurred in the Southern Hemisphere. Similarly, 81% and 75% of BTs below 173.15K and 178.15K, respectively, occur South of the Equator. The coldest MODIS BT was 165.6K, recorded

on December 31, 2018 ~620 km WNW of Tuvalu and a list of all BT clusters, defined as one or more cold BTs in a 10 km area, below 168.15K is given in Table ST3. Strikingly, out of the 26 cold BT clusters in the MODIS data set, 6 were recorded in a 3-day period in late December 2018 in the region of the cold VIIRS measurement discussed here. This emphasizes the key role played by the atypically cold tropopause at the time. We also note that there were as many clusters of BTs below 168K in the last 5 years of the data set (13 clusters between 2015 and 2020) as the first 10 years (2004–2014). Similarly, 50% of the 17,707 MODIS BTs below 173K and 30% of the 799,485 BTs below 178K occurred in the final 3 years of the data set (2017–2020).

Similar to VIIRS, however, MODIS is in LEO and hence passes over a given location at a fixed time each day. For Aqua, this is ~01:30 and 13:30 local time and over land these overpasses may not correspond to the peak in convective activity. Over ocean, the early morning overpass does correspond quite well to peak activity. Indeed, 84.2%, 83.8%, and 90.6% of BTs below 178K, 173K, and 168K, respectively, are detected in the 01:30 overpass. Despite the temporal limitation, a comparison with the lower spatial resolution Himawari data (Figure S4) shows that the MODIS data appear broadly representative of the spatial distribution of very low BTs for the Asia/Pacific region.

6. Conclusions

This study discusses a particularly cold set of cloud top temperatures associated with deep convective over-shoots in the South West Pacific on December 29, 2018 that culminated in a cloud top temperature of 161.9K being measured by the VIIRS sensor. Unlike other extremely cold temperatures that were driven by cyclonic storms, this event is the result of a very cold tropopause coupled with semi-organized convective activity that is relatively typical for the region. The success of VIIRS in identifying these extremely cold temperatures that are missed by other sensors highlights the benefits of the improved spatial resolution afforded by recent sensor developments, while the high temporal resolution of the AHI and ABI instruments used here exemplifies the use of geostationary sensors for analyzing convective storms, despite their limited spatial resolution.

15 years of data from the MODIS instrument gives insight into the spatial distribution of cold cloud tops, with the majority of such clouds occurring in the South Western Pacific, which has also been shown to be the region with the coldest tropopause temperatures in reanalysis data. This MODIS data set shows that cold cloud tops have become more common over 2004–2020 period, although this may be biased by the exceptionally cold clouds of late 2018. Further investigation is therefore required to determine if robust trends in cloud temperatures do exist, and how these link to changes in the tropopause and increasing sea surface temperatures.

Data Availability Statement

The processed data and source code used for analysis and figure generation are available on Zenodo: Simon Proud (January 14, 2021). [simonrp84/VIIRS_Supercold_BT](https://zenodo.org/record/5088844): Code as-used in GRL paper on VIIRS low BT measurements (Version v1.0). Zenodo. <https://doi.org/10.5281/zenodo.4441127>. The original satellite data are available from the respective satellite owners/operators. Please note that in most cases the satellite operators require (free) registration in order to access the data: VIIRS and ABI are downloadable from: <https://www.class.noaa.gov/>; Himawari data are available from: <http://himawari.diasjp.net/bin/himawari.cgi>; AGRI data can be downloaded via: <http://satellite.nsmc.org.cn/portalsite/default.aspx>; MODIS data are available via: <https://search.earthdata.nasa.gov/>; SLSTR data are downloadable at: <https://scihub.copernicus.eu/dhus/>; AVHRR data in GAC format from NOAA satellites are available from: <https://www.class.noaa.gov/>, while AVHRR data from the MetOp satellites is available via EUMETSAT: <https://eoportal.eumetsat.int/>.

Acknowledgments

Dr. S. R. Proud's work was supported by the Natural Environment Research Council, grant number NE/R013144/1. The authors wish to thank the VIIRS, AHI, and AGRI instrument teams for their thoughts and comments regarding calibration at extremely cold temperatures. The authors also thank the anonymous reviewers for their constructive and insightful comments on this manuscript.

References

- Aminou, D. (2002). Msg's sevir instrument. *ESA Bulletin*, 111, 15–17.
- Angal, A., Xiong, X., McIntire, J., Chen, N., & Oudrari, H. (2018). Prelaunch and on-orbit electronic calibration for earth-observing instruments. *Earth Observing Missions and Sensors*, 10781, 107811D. <https://doi.org/10.1117/12.2500057>

- Bachmeier, S. (2019). *Typhoon kammuri in the west Pacific Ocean, with record cold cloud-top temperatures. (Technical report)*. Madison, WI: Cooperative Institute for Meteorological Satellite Studies, University of Wisconsin–Madison. Retrieved from <https://cimss.ssec.wisc.edu/satellite-blog/archives/35120>
- Barnes, W. L., Xiong, X., & Salomonson, V. V. (2003). Status of terra modis and aqua modis. *Advances in Space Research*, 32(11), 2099–2106. [https://doi.org/10.1016/S0273-1177\(03\)90529-1](https://doi.org/10.1016/S0273-1177(03)90529-1)
- Basher, R. E., & Zheng, X. (1995). Tropical cyclones in the southwest pacific: Spatial patterns and relationships to southern oscillation and sea surface temperature. *Journal of Climate*, 8(5), 1249–1260. [https://doi.org/10.1175/1520-0442\(1995\)008<1249:TCITSP>2.0.CO;2](https://doi.org/10.1175/1520-0442(1995)008<1249:TCITSP>2.0.CO;2)
- Bedka, K., Murillo, E. M., Homeyer, C. R., Scarino, B., & Mersiovsky, H. (2018). The above-anvil cirrus plume: An important severe weather indicator in visible and infrared satellite imagery. *Weather and Forecasting*, 33(5), 1159–1181. <https://doi.org/10.1175/WAF-D-18-0040.1>
- Bessho, K., Date, K., Hayashi, M., Ikeda, A., Imai, T., Inoue, H., et al. (2016). An introduction to Himawari-8/9 – Japan's new-generation geostationary meteorological satellites. *Journal of the Meteorological Society of Japan*, 94(2), 151–183. <https://doi.org/10.2151/jmsj.2016-009>
- Coppo, P., Ricciarelli, B., Brandani, F., Delderfield, J., Ferlet, M., Mutlow, C., et al. (2010). SLSTR: A high accuracy dual scan temperature radiometer for sea and land surface monitoring from space. *Journal of Modern Optics*, 57(18), 1815–1830. <https://doi.org/10.1080/09500340.2010.503010>
- Doswell, C. A. (2001). Severe convective storms – an overview. In C. Doswell III (Ed.), *Severe convective storms*. Boston, MA: American Meteorological Society (pp. 1–26). <https://doi.org/10.1007/978-1-935704-06-5>
- Ebert, E. E., & Holland, G. J. (1992). Observations of record cold cloud-top temperatures in tropical cyclone Hilda (1990). *Monthly Weather Review*, 120(10), 2240–2251. [https://doi.org/10.1175/1520-0493\(1992\)120<2240:OORCCT>2.0.CO;2](https://doi.org/10.1175/1520-0493(1992)120<2240:OORCCT>2.0.CO;2)
- Hersbach, H., Bell, B., Berrisford, P., Hirahara, S., Horányi, A., Muñoz-Sabater, J., et al. (2020). The era5 global reanalysis. *Quarterly Journal of the Royal Meteorological Society*, 146(730), 1999–2049. <https://doi.org/10.1002/qj.3803>
- Hong, S., Shin, D.-B., Park, B., & So, D. (2016). Development of prototype algorithms for quantitative precipitation nowcasts from AMI onboard the geo-kompsat-2a satellite. *IEEE Transactions on Geoscience and Remote Sensing*, 54(12), 7149–7156. <https://doi.org/10.1109/TGRS.2016.2596293>
- Li, Y., Xiong, X., McIntire, J., Angal, A., Gusev, S., & Chiang, K. (2018). NOAA-20 VIIRS thermal emissive bands on-orbit performance. *Earth Observing Missions and Sensors*, 10781, 107810N. <https://doi.org/10.1117/12.2324515>
- Li, Y., Xiong, X., McIntire, J., & Wu, A. (2018). Impact of blackbody warm-up cool-down cycle on the calibration of aqua modis and s-npp viirs thermal emissive bands. *IEEE Transactions on Geoscience and Remote Sensing*, 56(4), 2377–2386. <https://doi.org/10.1109/TGRS.2017.2779105>
- Raspaud, M., Hoese, D., Dybbroe, A., Lahtinen, P., Devasthale, A., Itkin, M., et al. (2018). Pytrill: An open-source, community-driven python framework to process earth observation satellite data. *Bulletin of the American Meteorological Society*, 99(7), 1329–1336. <https://doi.org/10.1175/BAMS-D-17-0277.1>
- Schmit, T. J., Griffith, P., Gunshor, M. M., Daniels, J. M., Goodman, S. J., & Lebar, W. J. (2017). A closer look at the ABI on the goes-r series. *Bulletin of the American Meteorological Society*, 98(4), 681–698. <https://doi.org/10.1175/BAMS-D-15-00230.1>
- Schueler, C. F., Clement, J. E., Ardanuy, P. E., Welsch, C., DeLuccia, F., & Swenson, H. (2002). NPOESS VIIRS sensor design overview. *Earth Observing Systems VI*, 4483, 11–23. <https://doi.org/10.1117/12.453451>
- Smith, D., Barillot, M., Bianchi, S., Brandani, F., Coppo, P., Etzaluze, M., et al. (2020). Sentinel-3a/b slstr pre-launch calibration of the thermal infrared channels. *Remote Sensing*, 12(16), 2510. <https://doi.org/10.3390/rs12162510>
- Sun, L.-X., Zhuge, X.-Y., & Wang, Y. (2018). A contour-based algorithm for automated detection of overshooting tops using satellite infrared imagery. *IEEE Transactions on Geoscience and Remote Sensing*, 57(1), 497–508. <https://doi.org/10.1109/TGRS.2018.2857486>
- Teillet, P. M., Slater, P. N., Ding, Y., Santer, R. P., Jackson, R. D., & Moran, M. S. (1990). Three methods for the absolute calibration of the NOAA AVHRR sensors in-flight. *Remote Sensing of Environment*, 31(2), 105–120. [https://doi.org/10.1016/0034-4257\(90\)90060-Y](https://doi.org/10.1016/0034-4257(90)90060-Y)
- Zhou, S., & Cheng, J. (2020). An improved temperature and emissivity separation algorithm for the advanced himawari imager. *IEEE Transactions on Geoscience and Remote Sensing*, 58(10), 7105–7124. <https://doi.org/10.1109/TGRS.2020.2979846>
- Zhu, J., Shu, J., & Guo, W. (2020). Biases characteristics assessment of the Advanced Geosynchronous Radiation Imager (AGRI) measurement on board Fengyun-4A geostationary satellite. *Remote Sensing*, 12(18), 2871. <https://doi.org/10.3390/rs12182871>